

The Panopticon device: an integrated Paul-trap-hemispherical mirror system for quantum optics

G. Araneda,^{1,*} G. Cerchiari,¹ D. B. Higginbottom,² P. C. Holz,¹ K. Lakhmanskiy,¹ P. Obšil,³ Y. Colombe,¹ and R. Blatt^{1,4}

¹*Institut für Experimentalphysik, Universität Innsbruck, Technikerstrasse 25, 6020 Innsbruck, Austria*

²*Department of Physics, Simon Fraser University, Burnaby, British Columbia, V5A 1S6, Canada*

³*Department of Optics, Palacký University, 17. listopadu 12, 771 46 Olomouc, Czech Republic*

⁴*Institut für Quantenoptik und Quanteninformation, Österreichische Akademie der Wissenschaften, Technikerstrasse 21a, 6020 Innsbruck, Austria*

(Dated: November 25, 2021)

We present the design and construction of a new experimental apparatus for the trapping of a single Ba^+ ion in the center of curvature of an optical-quality hemispherical mirror. We describe the layout, fabrication and integration of the full setup, consisting of a high-optical access monolithic ‘3D-printed’ Paul trap, the hemispherical mirror, a diffraction-limited in-vacuum lens ($\text{NA} = 0.7$) for collection of atomic fluorescence and a state-of-the art UHV vessel. This new apparatus enables the study of quantum electrodynamics effects such as strong inhibition and enhancement of spontaneous emission, and achieves a collection efficiency of the emitted light in a single optical mode of 38 %.

I. INTRODUCTION AND MOTIVATION

Atomic ions confined and laser-cooled in Paul traps provide an experimental platform to study quantum objects with a unique level of control granted by the localization of the atomic wavefunction over a few nanometers, the long trapping time and the high fidelity manipulation of internal and external degrees of freedom [1]. These features have been used extensively to build quantum information processors (see for example Ref. 2), and for the study of fundamental phenomena in quantum optics and atomic physics (see for example Ref. 3).

One of the most fundamental and intriguing phenomena in quantum optics is the spontaneous emission and the possibility to modify it [4–7]. The spontaneous emission of atoms can be enhanced or inhibited in several ways. One way to modify the spontaneous emission rate is through dipole-dipole interactions between different atoms, namely sub- and superradiance-type effects [8–11]. This has been extensively studied in neutral atom systems and used for diverse applications (see for example Refs. 12–20). In general it is difficult to observe large modifications of the spontaneous emission with trapped ions using this approach, since the Coulomb interaction restricts the minimum achievable inter-ion distance. Nevertheless, some degree of modification has been shown for the case of two ions. In Ref. 21 enhancement of $\sim 1.5\%$ and inhibition of $\sim 1.2\%$ were observed by locating two ions 1470 nm away from each other.

Another way to enhance or reduce the rate of spontaneous emission of an atom is to modify the electromagnetic vacuum mode structure interacting with the atom [22, 23]. The electromagnetic mode structure can be altered by placing the atom close to dielectric interfaces [24], between two mirrors [25] or inside photonic structures producing a bandgap [26]. In particular, large enhancement of the emission from a single atom has been achieved using high-finesse cavities [27–30]. Recently, a five-fold enhancement in the sponta-

neous emission rate has been demonstrated by placing a single atom in a fiber cavity [31]. Furthermore, in the realm of solid state emitters, enhancement by a factor of more than 100 has been observed using microcavities [32]. In ion trap systems, strong coupling between a single trapped ion and a fiber cavity has been recently observed [33]. While a resonant cavity can increase the spontaneous emission rate into a particular mode, inhibiting the spontaneous emission requires to suppress the coupling to all modes. Only few experiments have demonstrated large inhibitions, see for example Ref. 34 where the rate of spontaneous emission of a single Rydberg atom was reduced by a factor ~ 20 , or Ref. 35 where the emission rate of a solid state emitter was reduced by a factor ~ 10 .

It is a common assumption in the field of cavity electrodynamics that full inhibition of the spontaneous emission can only be achieved by placing the atom between mirrors that cover the full solid angle around it, restricting all the vacuum modes resonant with the atom, see for example Ref. 6. However, given the point symmetry of the atomic emission, it is possible to fully control the emission rate by covering only *half* of the solid angle. This can be realized by placing the atom in the center of a concave hemispherical mirror, as theoretically predicted in Ref. 36. Taking this approach, both inhibition and enhancement of the spontaneous emission can be achieved depending on the distance R between the atom and the surface of the mirror, provided that the mirror is close enough to the atom to allow temporal interference of the field emitted in opposite directions. This condition can be written as $2R/c \ll 1/\Gamma$, where c is the speed of light and Γ is the free-space decay rate of the observed atomic transition. If $R = n\lambda/2$, where n is an integer and λ is the wavelength of the transition, an atom located in the center of curvature of the mirror is at a node of the vacuum mode density and inhibition is observed. Conversely, if the radius is $R = n\lambda/2 + \lambda/4$, an atom located in the center of curvature is at an anti-node, and enhancement is observed. If the mirror is not a hemisphere ($\text{NA} = 1$), but a spherical mirror with $\text{NA} < 1$ only a partial modification is expected. Fig. 1 shows the expected modification of the decay rate of a dipole transition depending on the numerical aperture of a perfectly reflective spherical mirror. Furthermore, in addition to the modification of the sponta-

* Corresponding author; gabriel.aranedamachuca@physics.ox.ac.uk; Current address: Department of Physics, University of Oxford

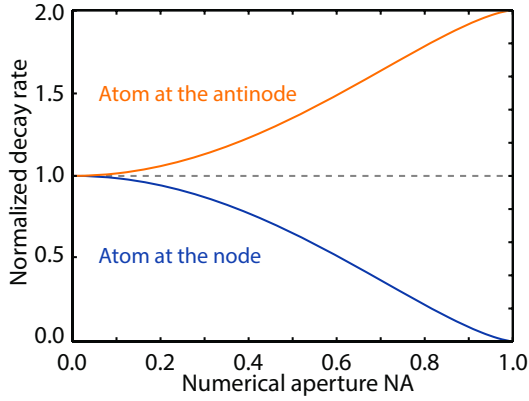


FIG. 1. **Modification of the spontaneous emission rate of an atom in the center of a hemispherical mirror.** The spontaneous emission of an atom at the center of curvature of a spherical mirror is inhibited or enhanced depending on the radius and numerical aperture of the mirror. If the radius of the mirror is $R = n\lambda/2$, the center of curvature is a node of the vacuum mode density and inhibition is expected (blue curve). If the radius of the mirror is $R = n\lambda/2 + \lambda/4$, the center of curvature is an anti-node of the vacuum mode density and enhancement is expected (orange curve). Full inhibition (resp. a doubling of the decay rate) is obtained when half of the space is covered by the mirror ($NA = 1$). In this plot a mirror with perfect reflectivity is assumed. Reproduced from Ref. 36.

taneous emission, a hemispherical mirror is predicted to lead to ground and excited state level shifts [36].

In this article we present the new ‘Panopticon’ [37] apparatus for the integration of a high-quality hemispherical mirror ($NA \approx 1$) and a Paul trap in order to realize the situation described above. In addition to the fundamental components of such a setup, i.e., the hemispherical mirror and a Paul trap, a high numerical aperture lens ($NA = 0.7$) is used to collimate the light emission and direct it to a detector, as shown in Fig. 2. The design and construction of such an apparatus presents multiple technical challenges which are discussed in the following:

- In section II A we discuss the construction and characterization of the hemispherical mirror. The effects discussed above vanish rapidly when the mirror deviates from a perfect hemisphere. The target RMS surface error for the fabricated mirror is $\lambda/10$ over the whole mirror surface. Furthermore, we describe how thermal expansion can be used to adjust the radius of the mirror in order to access both inhibition and enhancement of the spontaneous emission.
- In section II B we discuss the design and characterization of the high-NA lens used for light collection. The lens design aims at diffraction-limited performance, enabling interference and imaging experiments such as the ones presented in Refs. 38–40.
- In section II C we discuss the design of the Paul trap. The trap must provide full optical clearance between

the trapped ion and the hemispherical mirror. Additionally, it must provide optical clearance for the high-NA lens and for the required laser beams. Ideally, the trap design should allow to trap several ions simultaneously in a stable fashion and provide enough flexibility for multi-ion quantum optics experiments such as the one presented in Ref. 39.

- In section II D we discuss the integration of the mirror, trap and lens. The position of the optical elements should be adjustable in-situ, with nanometer precision.
- In section III we present the design of the vacuum vessel. All the above-mentioned elements have to be placed in an ultra high vacuum environment, which contains an atomic source and provides the required electrical connections and optical access.

Besides the fundamental interest in measuring effects predicted by quantum electrodynamics [36], being able to control the spontaneous emission of a dipole transition has several applications. For example, reducing the decay rate by two orders of magnitude on a dipole transition would increase the T_1 time of the transition up to microseconds, allowing the implementation of a qubit on such a transition. Using a dipole transition would be beneficial because it permits fast qubit control without the use of strong laser beams. Another application can be found in laser cooling, as tuning the decay rate of a dipole transition would allow to directly modify, e.g., the Doppler cooling rate [41, 42]. Furthermore, Doppler cooling typically needs repumper laser beams to depopulate additional states connected to the cooling transition [42]. By suppressing the spontaneous decay through these additional channels, it would be possible to Doppler cool without the need of repumping beams.

The system that we present here also provides high light collection efficiency. For an optimally oriented linear dipole, i.e., with its dipole moment oriented orthogonal to the optical axis used for collection, the expected photon collection efficiency is 38 % [43]. Remarkably, given the high quality of the overall optical system, with wavefront errors below $\lambda/10$ for all the components, the collected light can be captured in a single mode and coupled efficiently to a single mode fiber. The high collection efficiency and the cleanliness of the optical mode is expected to improve the signal to noise ratio of any optical measurement of atomic properties. Additionally, the improved collection and absorption rates enabled by this setup could be used to implement a quantum network without cavities [44, 45].

We note that some of the features exhibited by a setup employing a hemispherical mirror, such as high collection efficiency and improved single photon absorption, can be achieved using an atom in the focus of a parabolic mirror [46, 47]. Indeed, in Ref. 47 collection efficiencies as high as 54.8 % have been reported using a parabolic mirror. However, in this approach, the enhancement and inhibition of the spontaneous emission due to QED effects vanish for macroscopic parabolic mirrors [46]. Other approaches consist in using a combination of a high-NA lens collecting the light emitted by an atom and a mirror that retro-reflects the collected

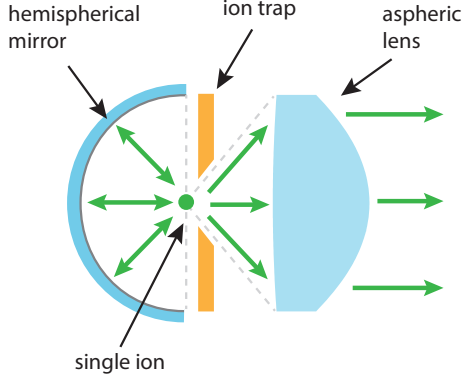


FIG. 2. **Main components of the Panopticon setup.** The green arrows show the propagation of the light emitted by the trapped atomic ion.

light. Although changes in the decay rates have been observed using this method [48], the modifications are limited by numerical apertures achievable in trapped ion systems for the collection lens. Furthermore, previous attempts to position an ion in the center of a spherical mirror have demonstrated stable trapping and improved light collection [49], but they have not achieved the mirror surface quality, radius tunability and numerical aperture required to show inhibition or suppression of the spontaneous emission.

II. THE PANOPTICON SETUP

The main feature of the Panopticon setup is the ability to confine a single trapped atomic ion in the center of a hemispherical mirror. The ion trap needs to provide full optical access between the trapped ion and the mirror. Additionally, in order to capture a large portion of the emitted field, a high-NA aspheric lens (NA = 0.7) is positioned opposite to the mirror, such that its focal point lies at the position of the ion. Therefore, the trap also needs to provide optical access for the solid angle captured by the asphere. Fig. 2 shows a schematic with the main components of the Panopticon setup. In the following sections we describe the design, construction and characterization of each of these main components, as well as their integration and positioning.

A. The hemispherical mirror

The main component of the Panopticon setup is the concave hemispherical mirror. Results about the fabrication and characterization of this mirror have been previously reported in Ref. 50. To observe a large modification of the spontaneous emission of an atom located in its center, the surface of the mirror can deviate only minimally from that of a sphere over its full numerical aperture. To our knowledge, the most precise macroscopic spherical objects ever fabricated are spheres with a surface deviation of only 17 nm peak-to-valley [51]. This

surface quality is achieved by randomly rotating the sphere between two polishing tools, for periods of several days. Unfortunately, this technique cannot be applied to concave spherical surfaces, and in general, until now, there was no technique able to produce a surface precision similar to that of a convex sphere.

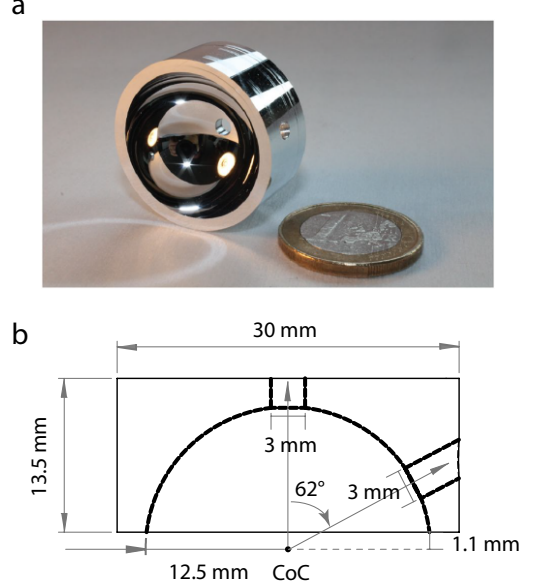


FIG. 3. **Fabricated hemispherical mirror.** **a.** Photograph of a fabricated hemispherical mirror. A euro coin is used for comparison. **b.** Schematic showing a cross section of the mirror with its relevant dimensions. Note the 3 mm diameter drilled holes which provide laser access to the center of curvature (CoC) of the mirror, where the ion will be located.

In collaboration with the Australian National University (ANU) we have produced hemispherical mirrors with RMS form errors consistently below 25 nm, a maximum peak-to-valley error of 88 nm, and a radius of curvature ≈ 12.5 mm. The mirrors were fabricated by diamond turning from a cylindrical aluminium 6061 substrate using a CNC (computer numerical control) nano-lathe [52]. To achieve low surface error, an in-situ white-light interferometer was implemented on the lathe, permitting the calibration of the tool with sub-nanometer precision prior to the machining. A detailed description of the fabrication and characterization of the mirrors can be found in Refs. 50 and 53.

Fig. 3 shows one of the fabricated mirrors, with a surface RMS error of 18.1 nm ($\lambda/27$ for $\lambda = 493$ nm) and a peak-to-valley error of 116.5 nm estimated using stitch interferometry (see Ref. 50 for details). Two drilled holes (3 mm diameter) provide laser access to the center of curvature, where the ion will be located (see Section II D). One of the holes is located along the optical axis of the mirror and the other at 62° with respect to the optical axis. The NA of the mirror is 0.996 (half aperture 85°), which is not a limitation of the fabrication process and is chosen such as to provide 1.1 mm optical clearance to the trapped ion. This gives laser access orthogonal to the

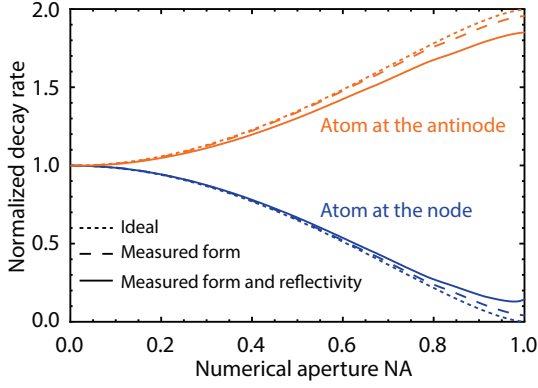


FIG. 4. **Expected performance of the fabricated mirror.** Modification of the spontaneous emission rate considering the achieved form, and the achieved form and reflectivity of the substrate. The numerical aperture $NA = 0.996$ is not distinguishable from $NA = 1.0$ in the plot. Considering form and reflectivity, the maximum expected enhancement and inhibition of the spontaneous emission rate correspond to 88 % of the ideal value. Reproduced from Ref. 50.

mirror's optical axis. The reflectivity of the mirror is set by the reflectivity of the substrate (0.92 for aluminium 6061 at 493 nm); it could be improved by applying a highly reflective thin film coating. However, the concave shape of the mirror makes it difficult to realize this in a uniform fashion, and special techniques would be required [54]. Fig. 4 shows the expected modification of the spontaneous emission considering the measured surface form, the reflectivity and the effect of the drilled holes. Considering form and reflectivity, the maximum expected enhancement and inhibition of the spontaneous emission rate in the 493 nm transition in $^{138}\text{Ba}^+$ correspond to 88 % of their ideal values. The main deviation from the ideal case comes from the limited reflectivity of the material.

The mirrors have been shown to be resilient to a cycle of vacuum bake-out under typical conditions (maximum temperature of 200 °C).

1. Temperature stabilization and tuning of the radius of curvature

To tune the radius of curvature of the mirror, we rely on the uniform thermal expansion of the substrate. The coefficient of thermal expansion of aluminium 6061 at room temperature is $23.5 \times 10^{-6} \text{ K}^{-1}$ [55]. A change in radius of curvature of $\lambda/4 \approx 123.3 \text{ nm}$ (with $\lambda = 493 \text{ nm}$) requires a temperature modification of 0.42 K. The mirror was heated while measured with a single-shot white-light ZYGO interferometer; this showed radius tunability over the desired range with no measured surface distortion due to thermal expansion. Nevertheless, small variations in environmental temperature in the experiment may lead to drifts of the radius of curvature, therefore, active stabilization of the temperature of the mirror is necessary.

To control and stabilize the temperature of the mirror we designed a resistively heated holder, shown in Fig. 5. The

holder is heated by applying current to a self-wrapped heating wire [56]. The temperature of the holder is measured in the back of the holder using two temperature sensors [57], which are glued to the holder [58]. The mirror is not in direct contact with the holder, it lies on ceramic rods [59] and glass spheres [60] (see Fig. 5), providing a distance of 1.1 mm between the outer surface of the mirror and the inside of the holder. This reduces the contact thermal conductivity between the mirror and the holder while maintaining the radiative heat transfer, and provides a homogeneous temperature over the volume of the mirror, albeit with a slow temperature tuning rate. The temperature is stabilized with a feedback loop using a high-precision PID [61]. In-vacuum tests have shown mirror temperature fluctuations below 1 mK over 10 hours, for different set points between 293 K and 303 K. The heating time constant of the mirror has been measured to be 5.39 hours, while the cooling time constant (cooling is achieved passively) is 3.89 hours. These times may be reduced by increasing the thermal contact between the mirror and the holder, which would, however, lower the temperature stability. The PID can be operated in sample and hold or constant current regime, which is useful for sensitive atomic measurements where a constant magnetic field could be required. The achieved temperature stability corresponds to fluctuations in the mirror's radius of curvature below 20 nm, that are lower than the measured surface error of the mirror.

B. The aspheric lens

To capture and collimate the light emitted by the ion, an aspheric lens is located opposite to the hemispherical mirror, as shown in Fig. 2. The main advantages of using an aspheric lens instead of a multi-lens objective are the simple, compact design and the reduced spherical and other optical aberrations. A low-aberration optical system is a crucial requirement for future experiments related to spatial properties of emitted and absorbed photons, for interference experiments with photons emitted by atoms in different traps coupled with optical fibers, as well as for optical detection of quantum features of atomic motion.

The asphere, designed and fabricated by Asphericon GmbH, has an $NA = 0.7$, a working distance of 9.60 mm and an effective focal length of 16.05 mm. The design was optimized using Zemax OpticStudio to achieve a diffraction-limited performance with ultra-low wavefront aberrations at 493 nm. The dimensions of the designed asphere are shown in Fig. 6. The surface facing the ion has a designed constant radius of curvature $R_B = 202.353 \text{ mm}$, whereas the opposite surface is a rotation symmetric asphere defined by the equation

$$z(r) = \frac{r^2}{R_F \left(1 + \sqrt{1 - (1+k) \frac{r^2}{R_F^2}} \right)} + \sum_{i=2}^8 A_{2i} r^{2i}. \quad (1)$$

The values of parameters R_F , k and A_{2i} are listed in Table I.

Three pieces of the designed asphere were fabricated using a S-TIH53 glass substrate [62], with refractive index $n_g \approx 1.87$

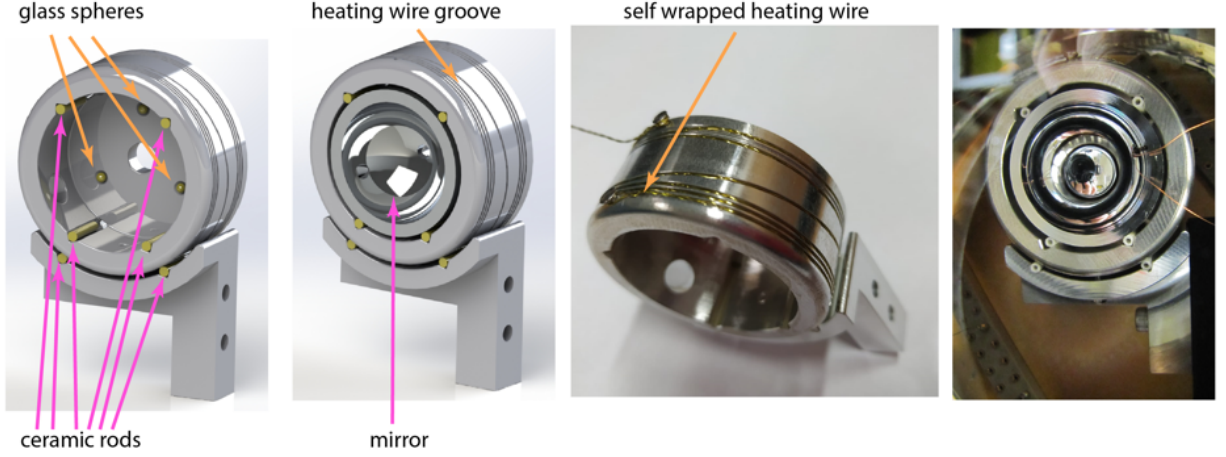


FIG. 5. **Mirror holder and heater.** Components of the mirror's aluminium holder and heater used to achieve a mirror temperature stability below 1 mK. The right-most photograph shows the setup used during the temperature stability tests performed in vacuum, with a thermistor attached directly to one of the mirrors.

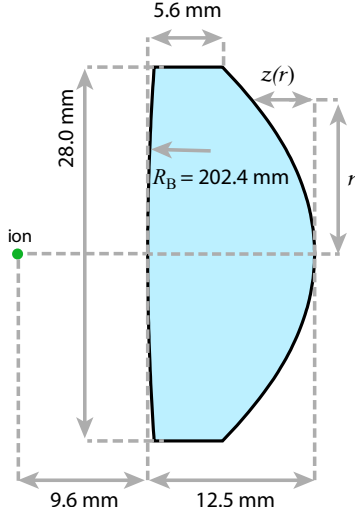


FIG. 6. **Aspheric lens dimensions.** The surface facing the ion is spherical with a radius of curvature R_B , whereas the aspheric surface is defined by Eq. (1). The ion is positioned 9.6 mm away from the front surface. The aspheric surface design parameters are listed in Table I.

($\lambda = 493$ nm) and Abbe number $v_g = 23.59$ ($\lambda = 546$ nm). The manufacturing process includes CNC grinding and polishing as a first step. Thereafter, ion beam figuring is used to reduce surface irregularities [63]. In this process, ion beams are directed at specific regions of the surface where surface errors have been detected. Finally, an anti-reflective coating for 493 nm is applied using plasma-assisted physical vapour deposition [64]. All these steps were performed by Asphericon GmbH. Fig. 7a shows a photograph of one of the aspheres and Fig. 7b shows the measured wavefront distortion [65]. RMS wavefront distortions below 37 nm ($\lambda/14$) and peak-to-valley distortions below 700 nm over the full numerical

TABLE I. Aspheric lens design parameters

Parameter	Value
R_F	14.56 mm
k	-0.776
A_4	$3.2022806 \times 10^{-6} \text{ mm}^{-3}$
A_6	$-2.9002661 \times 10^{-8} \text{ mm}^{-5}$
A_8	$-9.6249910 \times 10^{-11} \text{ mm}^{-7}$
A_{10}	$-1.0236456 \times 10^{-13} \text{ mm}^{-9}$
A_{12}	$4.5511459 \times 10^{-16} \text{ mm}^{-11}$
A_{14}	$3.3201252 \times 10^{-18} \text{ mm}^{-13}$
A_{16}	$-8.7645298 \times 10^{-21} \text{ mm}^{-15}$

aperture were achieved for the three aspheres. From Fig. 7b it is clear that the largest wavefront distortions occur close to the lens edge. In fact, by reducing the aperture of the lens to $\text{NA} = 0.65$, the RMS wavefront error is reduced to $\lambda/24$. The reflection from each coated surface was measured to be smaller than 0.4 % for incidence angles up to 40° , and the on-axis transmission of the lens was $\approx 95\%$, in agreement with the expected values. Both measurements were done with a laser beam with a 493 nm wavelength.

The lens is mounted in an aluminium holder, which allows for laser access to the focal point of the lens from several directions (see Section IID), and with negligible reduction of the numerical aperture.

C. The ion trap

The main challenge in the design of an ion trap compatible with the Panopticon setup is that the trap should provide full optical access not only between the trapped ion and the hemispherical mirror, but also between the ion and the aperture

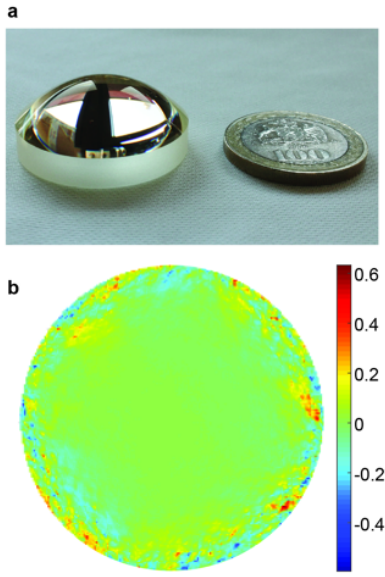


FIG. 7. **Fabricated aspheric lens.** **a.** Photograph of one of the three fabricated aspheric lenses together with a hundred Chilean pesos coin, giving the scale (the coin has a diameter of 23.25 mm). **b.** Measured wavefront distortion of one of the aspheres. Numbers in the color scale are in units of $\lambda = 493$ nm. Provided by Asphericon GmbH.

defined by the aspheric lens. This could be achieved using, for example, a needle trap [66]. However, this approach allows the trapping of only one ion without excess of micromotion. It is desirable to be able to trap several ions without micromotion, since the setup could then be used for a broader range of quantum optics experiments. Some comply partially with the criteria for optical access and stable trapping of several ions, including, for example, the miniaturized segmented “High Optical Access Trap 2.0” developed by Sandia National Laboratories [67]. However, this trap only possesses a clear aperture equivalent to $NA = 0.25$. The approach that we take here is the fabrication of a monolithic slotted pseudo-planar macroscopic trap. A simplified scheme of the trap geometry, with only the minimal electrode configuration needed to trap an ion, is shown in Fig. 8. Later in this article, we discuss the actual fabricated trap with additional features. In the design, an ion is trapped above the front surface, providing full clearance on the side of the hemispherical mirror and, through the slot, clearance corresponding to the numerical aperture $NA = 0.7$ of the aspheric lens. The geometry shown in Fig. 8 generates a confining RF pseudo-potential in the x and y directions, whereas trapping along the z direction is provided by the DC potential generated primarily by the DC electrodes DC1 and DC2. The DC voltages applied to the electrodes DC3, DC4, DC5 and DC6 contribute weakly to the trapping potential in the z direction and are meant for micromotion compensation. The ring shape of the RF electrode, although counter intuitive, is the result of a systematic optimization reducing the residual axial (z direction) pseudo-potential, allowing ion chains to be trapped with negligible axial micromotion.

The fabrication is done with subtractive 3D laser micro-

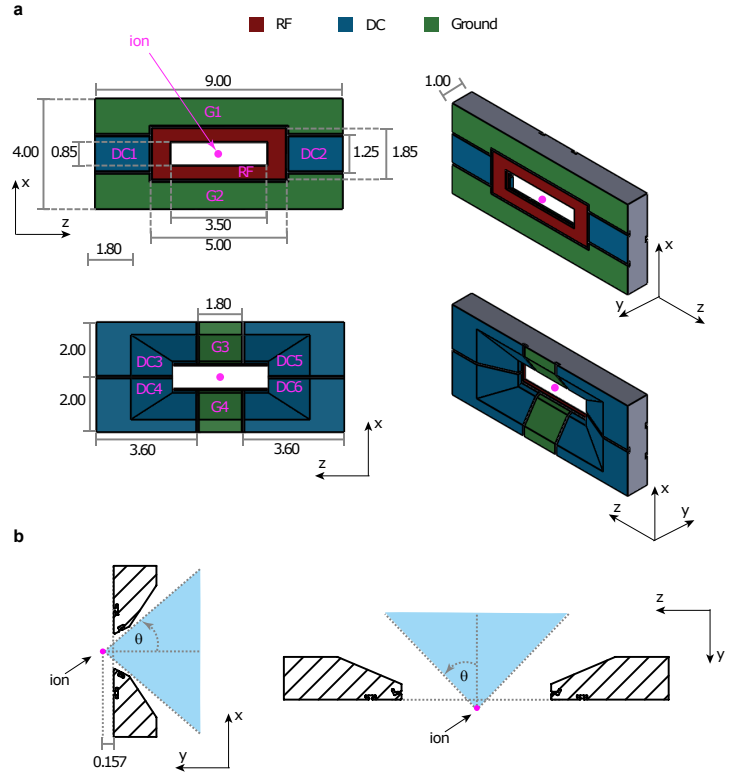


FIG. 8. **Ion trap design.** **a.** Simplified design of the trap. The RF, DC and ground (G) electrodes lie on the facets of a 3D-printed substrate. All dimensions in mm. White text indicates electrode names. **b.** Transverse cuts of the trap showing the optical clearance. The trap design provides full clearance towards the hemispherical mirror ($y > 0$). On the other side ($y < 0$), the optical clearance is slightly larger than required by the aspheric lens with $NA = 0.7$, corresponding to a $\theta = \arcsin(NA) \approx 44.4^\circ$ opening angle (blue area). The RF pseudo-potential minimum, and therefore the position of the ion, is located at a distance $y = 0.157$ mm from the front plane of the trap.

machining technology. The basic idea is to laser-machine a monolithic dielectric substrate to the required shape, including “trenches” separating different regions. In the following, we will refer to this technique as ‘3D-printing’. The surfaces are then coated with gold, creating an independent electrode in each region surrounded by trenches. Fig. 9 depicts how 3D-printing and coating are combined to create electrodes without the need for shadow masking and reduce the number of angled metal evaporation steps needed. The bottom of the carved trenches can be grounded or connected to one of the contiguous electrodes by shaping “ramps” between the bottom and the surface in the 3D-printing design.

The required precision of the dielectric substrate fabrication can be achieved by “laser carving” techniques provided by companies such as FEMTOprint S.A. in Switzerland or Translume Inc. in USA. The 3D-printing technology used by these companies employs strongly-focused high-energy laser pulses to locally change the physical structure of the substrate. A chemical process is then used to remove the treated material. Using this technique on, e.g., fused silica, the carved

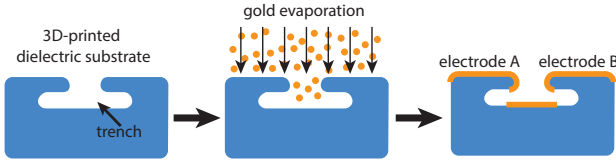


FIG. 9. **Electrode fabrication through 3D-printing and coating.** First, a dielectric substrate is “3D-printed” to create the trenches needed to separate electrodes. Then, the surfaces are coated with a conductor (gold) in an evaporation step. The profile of the trenches combined with the directionality of the evaporation step provides electric insulation between different regions, defining trap electrodes. The recess in the profile allows to apply evaporation from different angles without shorting the electrodes. The dimensions of the trench profile chosen for the fabricated trap are shown in Fig. 11d.

features can reach an average surface roughness below 100 nm, whereas the untouched surfaces can reach an average roughness below 5 nm. Additional polishing can reduce the roughness below 50 nm, though with detrimental effects in surrounding areas. A more detailed description of this technology applied to the fabrication of ion traps can be found in Ref. 68.

The conductive coating is applied in our clean room by means of electron beam evaporation of a thin layer of titanium (~ 2 nm), used as an adhesion layer, followed by a thick layer of gold (~ 200 nm). Gold evaporation is applied from three different angles on each side of the substrate. Gold electroplating could also be used afterwards to increase the thickness of the electrodes to $\sim 5 \mu\text{m}$.

1. Simulations of the trapping potential

The trap geometry presented in Fig. 8 is the result of a systematic optimization. The different dimensions and positions were varied to maximize the trapping frequencies for a $^{138}\text{Ba}^+$ ion, as well as the trap depth, and to reduce the trap capacitance and the residual axial RF field. The ion-electrode distance, which is constrained by the required optical clearance and laser access to the ion, was maximized. The electric potentials produced by the trap electrodes were simulated via finite element analysis using the software COMSOL Multiphysics 4.4. In these simulations the grounded hemispherical mirror was included.

Fig. 10 shows the total trapping potential. The RF pseudopotential minimum is located $157 \mu\text{m}$ away from the front plane of the trap, and the distance of a trapped ion to the closest electrode is $453 \mu\text{m}$. For comparison, in our current “Innsbruck-style” blade trap [69] this distance is $707 \mu\text{m}$. Small ion-electrode distances tend to increase the ion heating rate due to, e.g., surface noise [70]. Keeping this distance relatively large is therefore important.

Fig. 10c shows the trapping potentials along each coordinate axis. The potential is symmetric about the trap center along directions x and z , but not along y , as typically observed

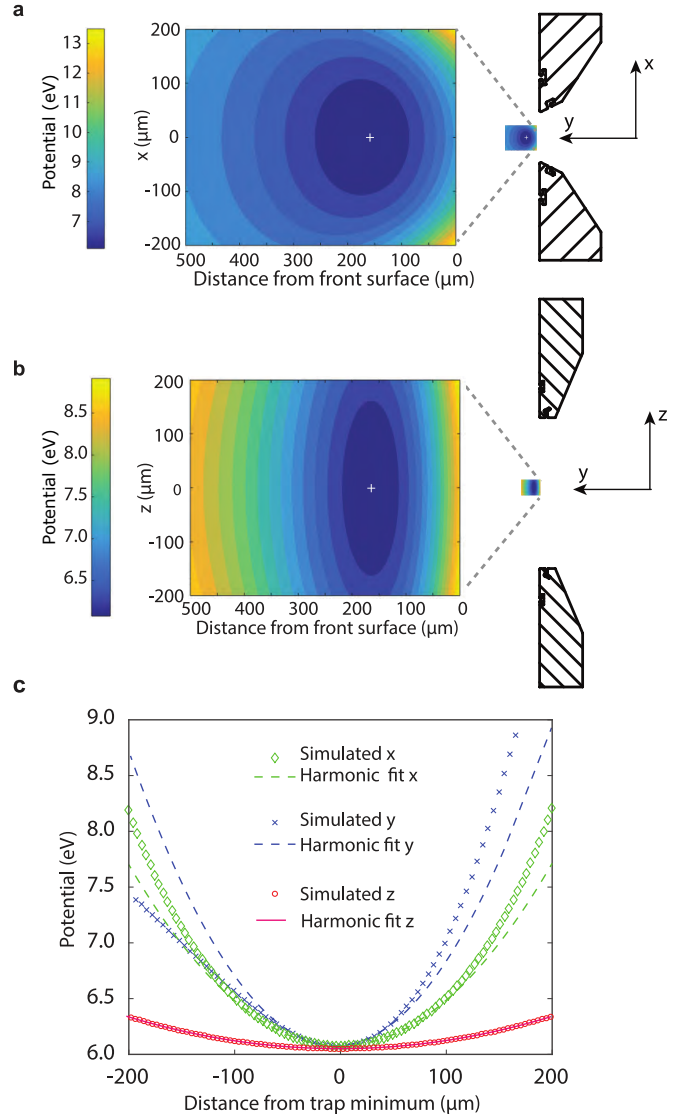


FIG. 10. **Simulated trapping potential.** The parameters are those of ‘config. 1’ in Table II. **a.** Cross section through the x - y plane. The white cross shows the position of the minimum. **b.** Cross section through the y - z plane. **c.** Trapping potential along the x , y and z axis. Close to the center, in a range of $\pm 50 \mu\text{m}$, the potentials are well approximated by harmonic potentials.

in surface traps [66]. The trapping frequencies can be varied with the voltages applied to the different electrodes. Table II shows the simulated trapping frequencies and trap depths obtained for a $^{138}\text{Ba}^+$ ion. The trap depths are in the eV regime, comparable with 3D rod or blade traps [71], which makes the trap suitable for operation at room temperature.

Simulations show that independent control of the voltages applied to the electrodes DC3, DC4, DC5 and DC6 is sufficient for compensation of micromotion in all directions. Further simulations with different trench geometries and dimensions were carried out. The most relevant trench parameter, i.e., the electrode-electrode separation provided by the trench, was varied between $50 \mu\text{m}$ and $150 \mu\text{m}$. Variations in this

TABLE II. Trap driving parameters and resulting trap frequencies and depths, obtained by finite elements simulations for $^{138}\text{Ba}^+$. Three different configurations are shown. DC1 and DC2 refer to the ‘endcap’ electrodes shown in Fig. 8, while DC3, DC4, DC5 and DC6 are the electrodes in the back plane. In these three configurations the electrodes G1, G2, G3, G4 and the mirror are grounded.

	config.1	config. 2	config. 3
RF freq. $\Omega_{\text{RF}}/2\pi$ (MHz)	16.0	16.0	16.0
RF amplitude U_{RF} (V)	1000	1500	2000
DC1,2 (V)	200	300	400
DC3,4,5,6 (V)	82	123	164
$\omega_x/2\pi$ (MHz)	1.33	2.16	2.96
$\omega_y/2\pi$ (MHz)	1.57	2.34	3.07
$\omega_z/2\pi$ (MHz)	0.51	0.62	0.72
Trap depth (eV)	2.4	4.9	8.2

range have negligible effect on the trapping potential, so that the final dimensions were selected based on breakdown test results described in the following section.

2. The fabricated trap

While the fabricated trap has the same core geometry as presented in Fig. 8, it includes additional features. Fig. 11 shows schematics and renders of the actual design. The ground electrodes G1 and G2 in the front plane are divided into smaller electrodes GR1, GR2, GR3 and GR4 (Fig. 11a) to add more flexibility for the compensation of micromotion. These electrodes, together with all other electrodes in the front plane (EC1, EC2, RF and GRB), are extended to reach the back plane. There, together with the back plane electrodes CU1, CU2, CU3, CD1, CD2 and CD3, they are prolonged into conductive traces extending beyond the radii of the hemispherical mirror and of the aspheric lens (Fig. 11b). This flat and elongated design provides enough space for wire-bonding, which connects the electrodes to the voltage supplies through a printed circuit board (PCB, see Section II C 3). In this way, the optical clearance to the trapping region is not affected by the bonding wires. The extended area is also used to mount the trap to an aluminum holder using through-holes.

Additionally, grooves in the front face are carved in the substrate (during the 3D-printing process). These grooves improve the clearance of the laser beams that propagate close to the surface, reducing the light scattered by the trap. This is of particular importance when addressing single ions using a strongly focused $1.7\ \mu\text{m}$ laser. The conical vertical grooves shown in Fig. 11a match the divergence of such a beam, with additional $100\ \mu\text{m}$ clearance from the point where the beam intensity has decayed by a factor of $1/e^2$. The horizontal cylindrical grooves give enough optical clearance for lightly focused axial cooling and optical pumping beams. Fig. 11c shows transverse cuts at the trap center, showing the position

of the ion and the optical clearance provided by the design. The dimension of the trenches separating adjacent electrodes, shown in Fig. 11d, were chosen after performing in-vacuum DC and RF breakdown tests on a simplified trap. The separation between electrodes varied between 50 and $150\ \mu\text{m}$. These tests did not show any sign of electric breakdown between electrodes with DC voltages as high as $700\ \text{V}$ and RF voltages as high as $1200\ \text{V}$ at $20\ \text{MHz}$. The separation was finally chosen to be $100\ \mu\text{m}$. The bottom of the trenches is connected to the common ground GR B. A complete 3D drawing of the designed trap can be found in the supplementary material. Fig. 12 shows a photograph of one of the traps fabricated by FEMTOprint S.A. before metalization.

We have performed simulations of the generated trapping potential for the fabricated trap design, including all the aforementioned features. The differences with the results of the simulations of the simplified version presented in section II C 1 are negligible.

3. Trap holder, in-vacuum low-pass filter and voltage driving

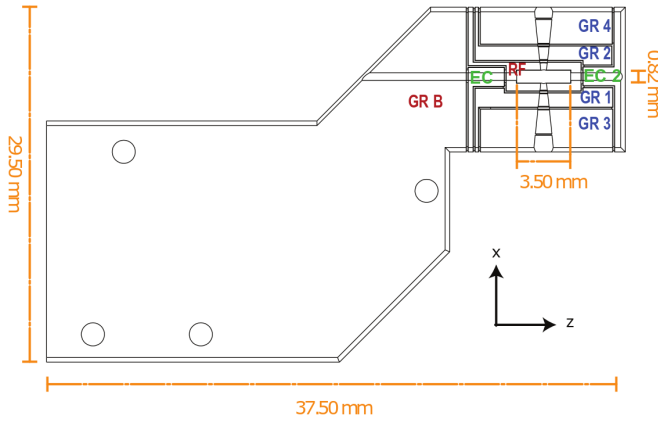
The ion trap is mounted on an aluminum holder plate ($2\ \text{mm}$ thickness) using three screws, as shown in Fig. 13a. The holder plate also acts as a heat sink for the trap and is contacted to the body of the vacuum chamber. This plate also holds a filter PCB. The trap is wire-bonded to the PCB using gold wires. The PCB, made of alumina [72] with a thickness of $1\ \text{mm}$, has 16 silk-printed gold traces, wire-bond pads, paths and soldering pads [73] for DC and RF routing. There are 8 vias to route some of the paths to the opposite side of the PCB. All the DC paths are capacitively coupled to a common ground using $1\ \text{nF}$ high voltage surface mounted capacitors [74], suppressing RF pick up. Additionally, $1\ \text{k}\Omega$ ex-vacuum resistors are used in order to filter high frequency noise induced in the DC electrodes (cutoff frequency $1\ \text{kHz}$). Fig. 13b and c show a schematic view of the PCB. At the edge opposite to the trap, the PCB has 16 gold pins [75] soldered [76], allowing easy connection and disconnection of each line to copper wires attached to the electrical feedthroughs on the base vacuum flange (Fig. 15). None of the PCB traces or the wires are exposed to the atomic flux from the atom source (see section III A).

The DC voltages are generated outside the vacuum chamber using a high-precision high-voltage source [77]. The RF voltage is generated using a high-precision signal generator [78] followed by a $28\ \text{dB}$ amplifier [79] and a helical resonator [80].

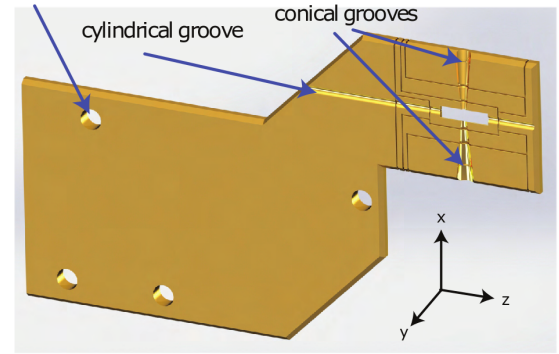
D. System integration

The optical setup, consisting of the hemispherical mirror, the aspheric lens and the ion trap, has to be set in place in a robust and stable manner, while still providing enough degrees of freedom for correct alignment. The holders and positioners have to be compatible with the ultra-high vacuum environment needed to trap single atomic ions in a stable way. To do

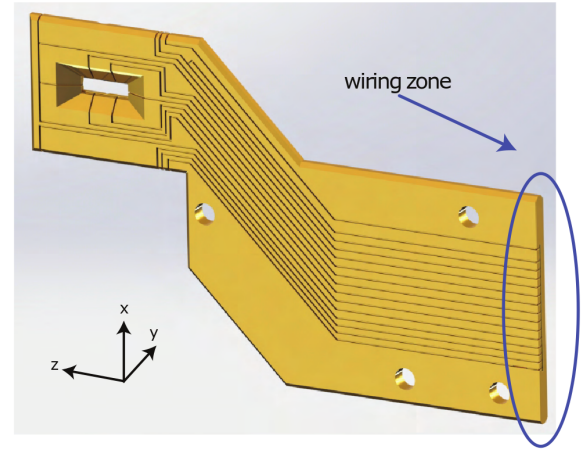
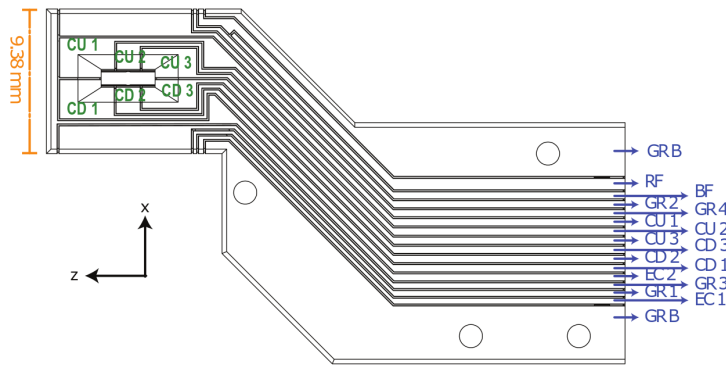
a) Front view



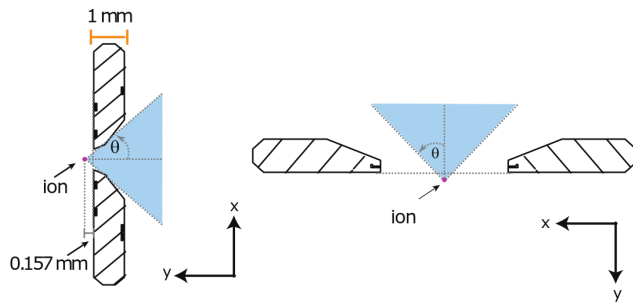
drilled holes



b) Back view



c) Transversal cut



d) Trenches dimensions

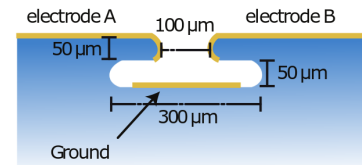


FIG. 11. Full design of the ion trap. **a.** Front side of the final trap design. Cylindrical and conical grooves are carved in the substrate in order to minimize the scatter of laser beams propagating close to the surface. All front electrodes extend to the back plane via the edges of the trap. **b.** In the back plane all the electrodes are extended to one extremity of the substrate, where wire-bonding is used for connection to voltage supplies. **c.** Transverse cut at the trap center showing the optical clearance provided by the trap. **d.** Dimensions of the trenches separating the electrodes.

so, we designed the mounting system shown in Fig. 14. In this setup, all the elements are carefully designed in order to provide the optical clearance required by the mirror and the lens, and laser access. The positions of the mirror and the lens can be set independently using xyz -nanopositioners [81] shown in the figure. The positioners have a step size of 1 nm in each di-

rection, a position readout resolution of 1 nm and a maximum displacement of 12 mm.

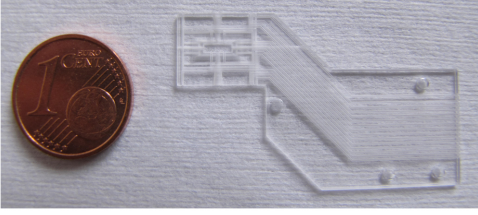


FIG. 12. **Fabricated ion trap.** Fabricated ion trap before metalization.

III. THE VACUUM VESSEL

The Panopticon optical setup is placed in an ultra-high vacuum environment. The vacuum vessel, shown in Fig. 15, is build around an 8"-CF spherical octagon chamber [82].

A customized 6-way cross is attached to the main chamber, providing enough flanges to connect a vacuum valve [83], a vacuum gauge [84], the electric feedthroughs for the wiring of the nanopositioners, a non-evaporable getter (NEG) pump [85] and a viewport. The main pumping is done with a combined ion and NEG pump [86] attached to the main chamber. During the NEG activation, the pump can reach temperatures close to 450°C. This temperature is not compatible with the maximum temperature to which the nanopositioners can be exposed (150°C). In order to avoid damaging the nanopositioners, the pump is retracted from the main chamber using a spacer, and a two-layer aluminium heat shield is placed between the pump and the positioners (see Fig. 15). According to simulations performed by the pump manufacturer this is sufficient to prevent damage of the nanopositioners.

The vacuum vessel has all the necessary viewports to provide laser access to the center of the trap using the planned beam directions (see Fig. 14), including a CF-160 viewport on the top of the chamber. All the viewports [87] are anti-reflection coated for all the wavelengths needed to load, cool and control $^{138}\text{Ba}^+$ ions, i.e, 413, 493, 614, 650 and 1762 nm. For these wavelengths the reflectivity is below 1 %. The viewport used for transmitting the light emitted by the ion and collimated by the aspheric lens has an optical quality surface, with wavefront aberrations below $\lambda/10$ over all the surface (with $\lambda = 493$ nm) [88]. An additional Germanium viewport [89] is attached to the main chamber, to allow monitoring of the temperature of the atom oven using a thermal camera outside the chamber (see Section III A).

The electrical connections needed to drive the ion trap, to heat an atom dispenser oven and to measure and control the temperature of the mirror are routed through feedthroughs in the customized CF-160 bottom flange. This customized flange also has a CF-16 viewport intended for 1.7 μm laser addressing of individual trapped ions.

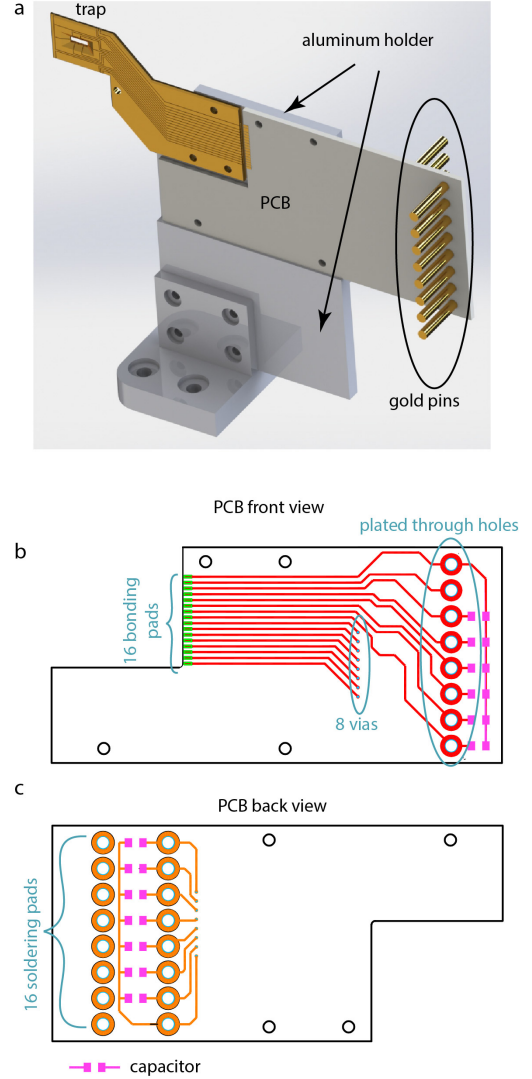


FIG. 13. **Trap holder and filter PCB.** Both the trap and the PCB filter are mounted on an aluminum holder. The trap is wire-bonded to the PCB which has conducting paths, capacitors and pins for connection to the DC and RF sources.

A. Atom source

To provide a source of atoms inside the vacuum chamber, we have designed a loading stage that simultaneously contains a resistively heated Ba dispenser oven and a laser ablation target. The resistively heated oven is a reliable way to produce a flux of neutral atoms in the center of the trap, which can then be ionized using a 413 nm laser through a two-step excitation process. This process is, however, slow, and produces an excess of heat inside the vacuum chamber that can have detrimental effects on the operation of ion traps, such as undesired thermal expansion of the electrodes and thermal expansion of the hemispherical mirror.

Laser ablation from a target is an alternative method which has been proved to be more efficient and less detrimental to

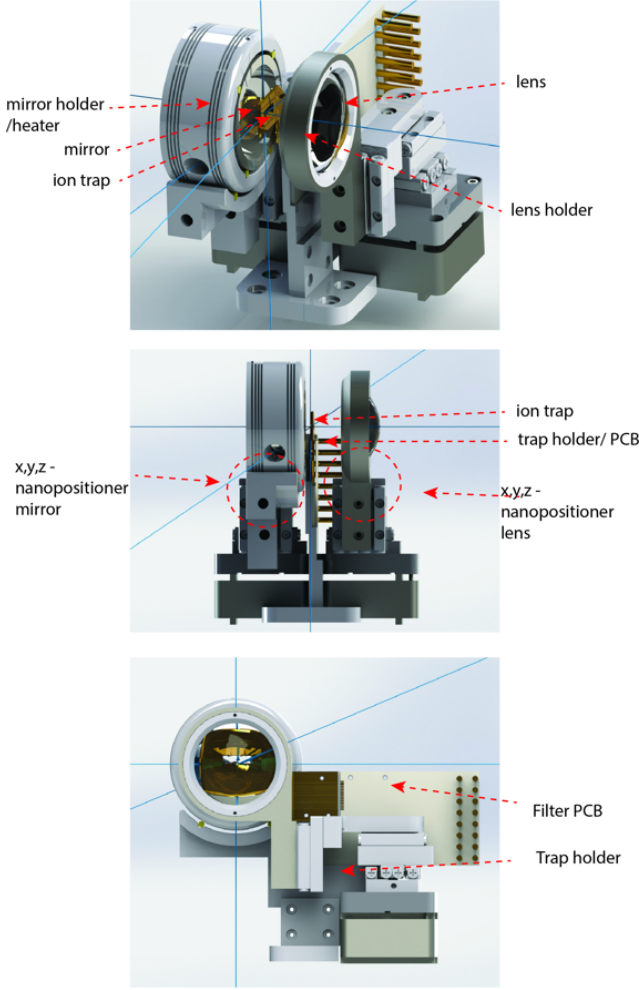


FIG. 14. **Panopticon optical setup.** The mirror and lens are mounted on independent xyz -nanopositioners, whereas the position of the ion trap is fixed. The blue lines show the four laser axes.

ion trap operation (see for example Ref. 90). In this approach, short and strong laser pulses are applied on a Ba target to produce neutral and ionized atoms, which eventually reach the center of the trap. It has been experimentally shown that instead of using a pure Ba target, targets containing BaTiO_3 or BaO produce higher Ba^+ yields [91], making loading more efficient while lifting the requirement of an additional photo-ionization laser. At the same time, using BaTiO_3 instead of pure Ba prevents fast oxidation of the sample during preparation of the vacuum setup.

Fig. 16 shows the designed loading stage, where both a resistive dispenser oven [92] and a BaTiO_3 ablation target [93] are located. The holder is made of macor[®] ceramic, which exhibits a low thermal and electric conductance. Both the target and the oven are enclosed in a copper shield, which simultaneously acts as a thermal radiation shield and prevents the ablated Barium from coating surfaces in the chamber and in the trap. Two circular apertures in the front with 1 mm diam-

eter, one for each atom flux production process, are used to collimate the atomic flux towards the center of the ion trap. As the ablation process spreads atoms in every direction, a mirror and a hole in the shield are used (Fig. 16). This configuration prevents a high atomic flux from exiting the shield and directly coating the top CF-160 viewport used for the ablation laser beam. Additionally, there is a small square aperture in the side of the stage, which allows for monitoring of the oven temperature with a thermal camera through an infra-red transmissive Germanium viewport. This can be used to characterize the heating dynamics of the oven in ultra-high vacuum and to optimize the loading process avoiding excess heating [94].

A broad range of pulsed laser sources can produce the pulses needed for ablation. An example of such a source is a pulsed diode pumped solid state laser (DPSS), with a wavelength of 515 nm and energy per pulse of 170 μJ [95]. This wavelength is compatible with our coated viewports.

B. Vacuum preparation and ex-vacuum elements

The cleaning of all the vacuum components is done following the procedure described in Ref. 96. The main components of the vacuum chamber are pre-bake at 450 $^{\circ}\text{C}$, whereas when adding the in-vacuum optical system and the nanopositioners, the system must be baked at 150 $^{\circ}\text{C}$.

Three pairs of magnetic field coils are attached to the outside of the main chamber flanges in order to provide a homogeneous magnetic field at the center of the trap. These coils may be replaced by rings of permanent magnets in order to achieve a better suppression of RF magnetic field noise. Four legs are attached to the exterior of the vacuum chamber to support it on an optical table.

IV. SUMMARY AND OUTLOOK

In this article we have presented the design and construction of a new setup which will allow us to study quantum electrodynamics effects. Furthermore, the setup features an unprecedented single-mode collection efficiency. We have presented the design and construction of the main optical components of the setup, namely a hemispherical mirror and an aspheric lens, and shown how the strict requirements on their optical performance can be fulfilled. Both the mirror and the lens achieve a wavefront distortion below $\lambda/10$.

The fabrication of macroscopic concave hemispherical mirrors with unprecedented precision will give us access to enhancement and inhibition of the spontaneous emission of a single atom of more than 96 % of its free-space value. The fabrication technique could be extended to obtain other concave surfaces, allowing for more exotic quantum electrodynamics situations. One example would be a hemispherical mirror with a $\lambda/4$ radius step as shown in Fig. 17 (details can be found in Ref. 97). Such a mirror could be used to enhance the spontaneous emission in the modes collected by a lens, while inhibiting the rest, resulting in collection efficiencies close to 100 % for a perfectly shaped mirror. For a mirror with a $\lambda/4$

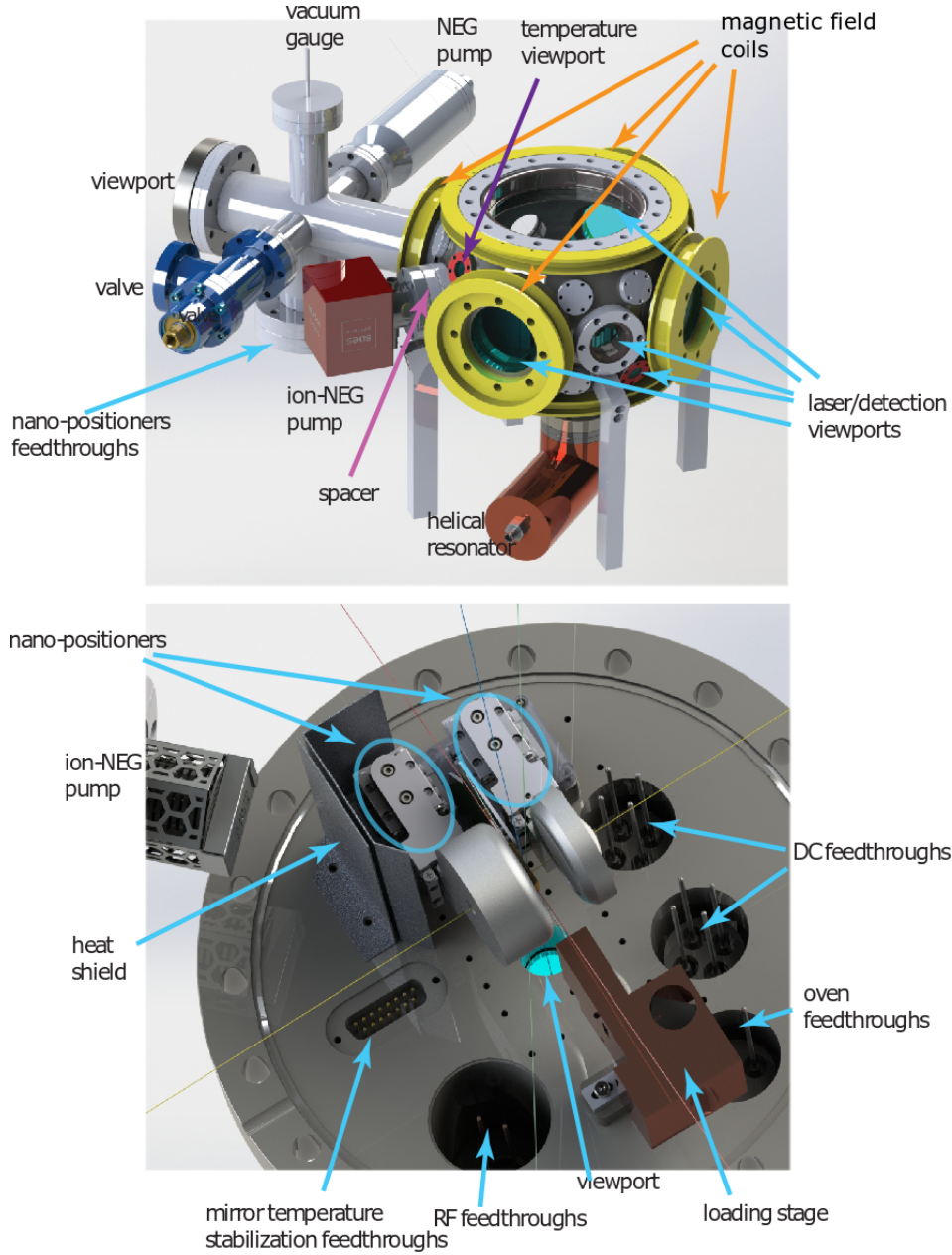


FIG. 15. **Main components of the vacuum vessel.** See details in the main text.

step, fabricated with the surface accuracy demonstrated in section II A, combined with the $NA = 0.7$ lens presented in section II B, an unprecedented 75 % single-mode collection efficiency is expected [53].

We have also presented the design of a monolithic high optical access ion trap. Such a trap provides the optical access required for the observation of the quantum electrodynamics effects described above. The trapping parameters are similar to those in state of the art macroscopic traps, such as our “Innsbruck-style” blade trap [69]. The design of this new trap employs 3D-printing technologies. The basic concept of using trenches to separate electrodes can be extended to more complex trap geometries, including segmented traps or traps

designed for trapping of 2D or 3D ion crystals, with high optical access to the trapped particles. The trap fabrication process does not require alignment of different parts nor shadow masking, which makes it reliable and repeatable. The exceptionally high optical access achieved by the trap could also be used in ion setups that integrate an optical cavity [98, 99].

We have also presented the design of the complete setup, which includes a state of the art vacuum vessel and an assembly for fast loading of ions in the trap via laser ablation. With several of these setups one could perform experiments related to remote entanglement distribution and quantum networking without optical cavities [44, 45].

The physical phenomena that we aim to study with this

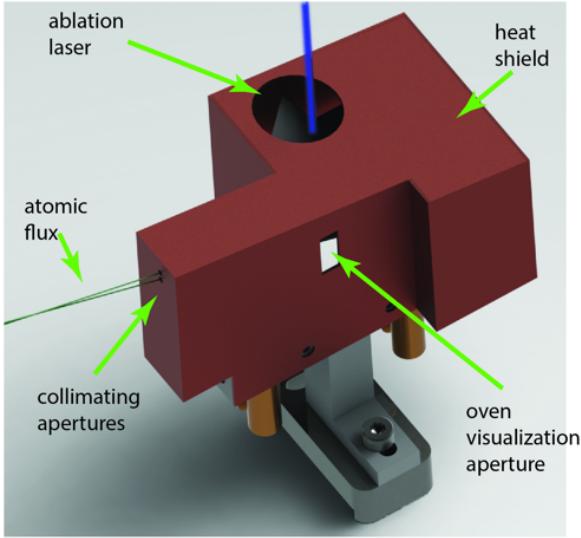
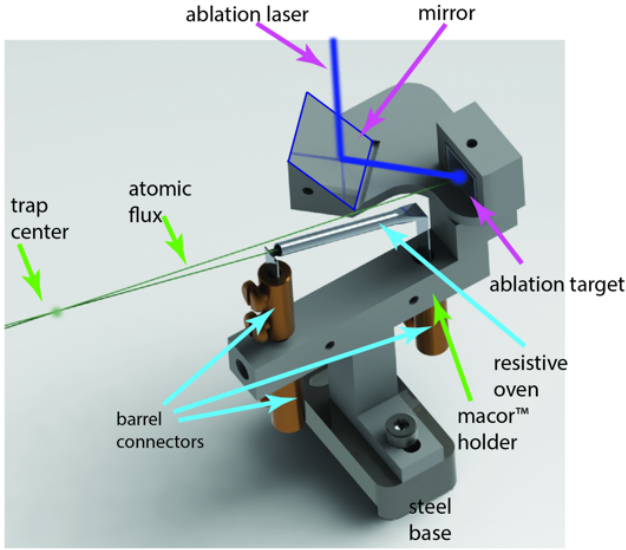


FIG. 16. **Loading stage.** Design of a loading stage combining a resistive Barium dispenser oven and a target for laser ablation. See details in the main text.

setup, such as strong inhibition and enhancement of the spontaneous emission, are not restricted to atomic ions, but could be observed from any quantum emitter. The optical setup presented here could be used with other systems with promising prospects in quantum networking and communications, such as quantum dots or diamond spin qubits [100, 101].

ACKNOWLEDGMENTS

We thank Christoph Wagscheider and the rest of our mechanical workshop team for their advice and help with the fabrication of the mechanical components. We gratefully acknowledge the contribution of W. Shihua and colleagues at the National Metrology Centre, A*STAR in Singapore. Without

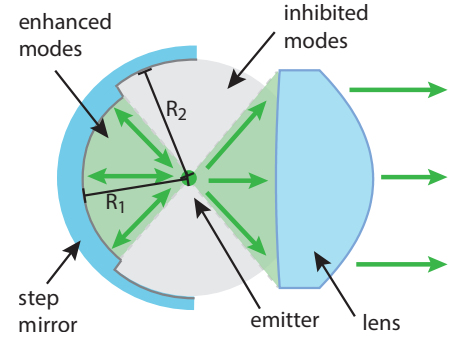


FIG. 17. **Step mirror concept.** A mirror with radius of curvature $R_1 = n\lambda/2$ around the center and $R_2 = n\lambda/2 + \lambda/4$ in the periphery would enhance the emission of photons in the solid angle collected by the lens while inhibiting the emission of uncollected light.

their expertise and the use of their high-NA optical interferometer and contact-probe measurements the first stages of this work would not have been possible. We also thank the FEMTOprint, Elceram and Asphericon teams for their advice and collaboration. We thank Lukas Slodicka, Martin Van Mourik, Pavel Hrmo, Ezra Kassa, Simon Ragg and Chiara Decaroli for fruitful discussions. This work was supported by the European Commission through project PIEDMONS 801285 and by the Institut für Quanteninformation GmbH. This work was supported by the European Commission also through the Marie Skłodowska-Curie Action, Grant Number: No 801110 (Erwin Schrödinger Quantum Fellowship Programme).

-
- [1] D. Leibfried, R. Blatt, C. Monroe, and D. Wineland, *Reviews of Modern Physics* **75**, 281 (2003).
 - [2] P. Schindler, D. Nigg, T. Monz, J. T. Barreiro, E. Martinez, S. X. Wang, S. Quint, M. F. Brandl, V. Nebendahl, C. F. Roos, *et al.*, *New Journal of Physics* **15**, 123012 (2013).
 - [3] B. Appasamy, J. Eschner, Y. Stalgies, I. Siemers, and P. Toschek, *Physica Scripta* **1995**, 278 (1995).
 - [4] P. A. M. Dirac, *Proceedings of the Royal Society of London. Series A, Containing Papers of a Mathematical and Physical Character* **114**, 243 (1927).
 - [5] T. A. Welton, *Physical Review* **74**, 1157 (1948).
 - [6] D. Kleppner, *Physical Review Letters* **47**, 233 (1981).
 - [7] P. W. Milonni, *American Journal of Physics* **52**, 340 (1984).
 - [8] R. H. Dicke, *Physical Review* **93**, 99 (1954).
 - [9] M. Gross and S. Haroche, *Physics Reports* **93**, 301 (1982).
 - [10] A. V. Andreev, V. I. Emel'yanov, and Y. A. Il'inskii, *Soviet Physics Uspekhi* **23**, 493 (1980).
 - [11] M. G. Benedict and E. D. Trifonov, "6.2 superradiance," in *Laser Fundamentals. Part 2*, edited by H. Weber, G. Herziger, and R. Poprawe (Springer Berlin Heidelberg, Berlin, Heidelberg, 2006) pp. 67–81.
 - [12] N. Skribanowitz, I. Herman, J. MacGillivray, and M. Feld, *Physical Review Letters* **30**, 309 (1973).
 - [13] C. H. van der Wal, M. D. Eisaman, A. André, R. L. Walsworth, D. F. Phillips, A. S. Zibrov, and M. D. Lukin, *Science* **301**, 196 (2003).
 - [14] A. Kuzmich, W. Bowen, A. Boozer, A. Boca, C. Chou, L.-M. Duan, and H. Kimble, *Nature* **423**, 731 (2003).
 - [15] R. Reimann, W. Alt, T. Kampschulte, T. Macha, L. Ratschbacher, N. Thau, S. Yoon, and D. Meschede, *Physical review letters* **114**, 023601 (2015).
 - [16] C. Chou, S. Polyakov, A. Kuzmich, and H. Kimble, *Physical Review Letters* **92**, 213601 (2004).
 - [17] A. T. Black, J. K. Thompson, and V. Vuletić, *Physical review letters* **95**, 133601 (2005).
 - [18] H. W. Chan, A. T. Black, and V. Vuletić, *Physical review letters* **90**, 063003 (2003).
 - [19] M. Wolke, J. Klinner, H. Keßler, and A. Hemmerich, *Science* **337**, 75 (2012).
 - [20] J. G. Bohnet, Z. Chen, J. M. Weiner, D. Meiser, M. J. Holland, and J. K. Thompson, *Nature* **484**, 78 (2012).
 - [21] R. DeVoe and R. Brewer, *Physical Review Letters* **76**, 2049 (1996).
 - [22] E. M. Purcell, H. C. Torrey, and R. V. Pound, *Physical Review* **69**, 37 (1946).
 - [23] M. Kiffner, M. Macovei, J. Evers, and C. Keitel (Elsevier, 2010) pp. 85 – 197.
 - [24] K. Drexhage, *Journal of Luminescence* **1**, 693 (1970).
 - [25] S. Haroche and D. Kleppner, *Physics Today* **42**, 24 (1989).
 - [26] G. Kweon and N. Lawandy, *Optics Communications* **118**, 388 (1995).
 - [27] M. Brune, P. Nussenzveig, F. Schmidt-Kaler, F. Bernardot, A. Maali, J. Raimond, and S. Haroche, *Physical Review Letters* **72**, 3339 (1994).
 - [28] D. Heinzen and M. Feld, *Physical Review Letters* **59**, 2623 (1987).
 - [29] C. Hood, T. Lynn, A. Doherty, A. Parkins, and H. Kimble, *Science* **287**, 1447 (2000).
 - [30] A. Kreuter, C. Becher, G. Lancaster, A. Mundt, C. Russo, H. Häffner, C. Roos, J. Eschner, F. Schmidt-Kaler, and R. Blatt, *Physical Review Letters* **92**, 203002 (2004).
 - [31] J. Gallego, W. Alt, T. Macha, M. Martinez-Dorantes, D. Pandey, and D. Meschede, *Physical review letters* **121**, 173603 (2018).
 - [32] K. J. Vahala, *Nature* **424**, 839 (2003).
 - [33] H. Takahashi, E. Kassa, C. Christoforou, and M. Keller, *Physical Review Letters* **124**, 013602 (2020).
 - [34] R. G. Hulet, E. S. Hilfer, and D. Kleppner, *Physical Review Letters* **55**, 2137 (1985).
 - [35] M. Bayer, T. Reinecke, F. Weidner, A. Larionov, A. McDonald, and A. Forchel, *Physical Review Letters* **86**, 3168 (2001).
 - [36] G. Hétet, L. Slodička, A. Glätzle, M. Hennrich, and R. Blatt, *Physical Review A* **82**, 063812 (2010).
 - [37] The Panopticon setup owes its name to a type of institutional building proposed by the English philosopher and social theorist Jeremy Bentham [102]. In this building, a single watchman located in a central tower can observe all the inmates of the institution, which are located in cells with optical clearance around the tower. Michel Foucault notably used the Panopticon as a metaphor for the modern surveillance state [103].
 - [38] P. Obšil, A. Lešundák, T. Pham, G. Araneda, M. Čížek, O. Číp, R. Filip, and L. Slodička, *New Journal of Physics* **21**, 093039 (2019).
 - [39] G. Araneda, D. B. Higginbottom, L. Slodička, Y. Colombe, and R. Blatt, *Physical Review Letters* **120**, 193603 (2018).
 - [40] G. Araneda, S. Walser, Y. Colombe, D. B. Higginbottom, Y. Volz, R. Blatt, and A. Rauschenbeute, *Nature Physics* **15**, 17 (2019).
 - [41] Y. Castin, H. Wallis, and J. Dalibard, *JOSA B* **6**, 2046 (1989).
 - [42] H. J. Metcalf and P. van der Straten, *JOSA B* **20**, 887 (2003).
 - [43] K. D. Sattler, *Handbook of nanophysics: nanoparticles and quantum dots* (CRC press, 2016).
 - [44] D. Hucul, I. V. Inlek, G. Vittorini, C. Crocker, S. Debnath, S. M. Clark, and C. Monroe, *Nature Physics* **11**, 37 (2015).
 - [45] L. Stephenson, D. Nadlinger, B. Nichol, S. An, P. Drmota, T. Ballance, K. Thirumalai, J. Goodwin, D. Lucas, and C. Ballance, *Physical Review Letters* **124**, 110501 (2020).
 - [46] G. Alber, J. Bernád, M. Stobińska, L. Sánchez-Soto, and G. Leuchs, *Physical Review A* **88**, 023825 (2013).
 - [47] R. Maiwald, A. Golla, M. Fischer, M. Bader, S. Heugel, B. Chalopin, M. Sondermann, and G. Leuchs, *Physical Review A* **86**, 043431 (2012).
 - [48] J. Eschner, C. Raab, F. Schmidt-Kaler, and R. Blatt, *Nature* **413**, 495 (2001).
 - [49] G. Shu, M. Dietrich, N. Kurz, and B. Blinov, *Journal of Physics B: Atomic, Molecular and Optical Physics* **42**, 154005 (2009).
 - [50] D. B. Higginbottom, G. T. Campbell, G. Araneda, F. Fang, Y. Colombe, B. C. Buchler, and P. K. Lam, *Scientific Reports* **8**, 221 (2018).
 - [51] J. Turneare, C. Everitt, B. Parkinson, D. Bardas, J. Breakwell, S. Buchman, W. Cheung, D. Davidson, D. DeBra, W. Fairbank, *et al.*, *Advances in Space Research* **9**, 29 (1989).
 - [52] Nanotech 250UPL, Moore Precision Tools.
 - [53] D. B. Higginbottom, *Atom-light couplers with one, two and ten billion atoms*, Ph.D. thesis, Australian National University (2018).
 - [54] New developments in Atomic Layer Deposition (ALD) have shown promising results in uniform coating of complex 3D structures, making it possible to reach reflectivities close to 100 % without affecting the precision of the mirror surface. See for example <https://www.laseroptik.de/en/>

- coating-guide/production-methods/ald.
- [55] D. E. Hodgson, M. Wu, and R. J. Biermann, “Asm handbook, volume 2, properties and selection, nonferrous alloys and special-purpose materials,” (1990).
 - [56] Insulated nichrome wires, LakeShore Cryotronics® NC-32.
 - [57] NTC Thermistors BC101B1K, Littelfuse®.
 - [58] In these tests a silver-filled epoxy is used, Kurt J. Lesker KL-325K.
 - [59] Ceramic tube Allectra 358S-TUBE-20, diameter 2 mm.
 - [60] Glass sphere diameter 2 mm.
 - [61] BelektroniG BTC-LAB-A2000.
 - [62] Ohara Corporation, quoted transmission of 0.951 % at 488 nm. Data sheet at <https://www.oharacorp.com/pdf/estih53.pdf>.
 - [63] X. Xie and S. Li, Handbook of Manufacturing Engineering and Technology, 1 (2013).
 - [64] J. M. Schneider, S. Rohde, W. D. Sproul, and A. Matthews, Journal of Physics D: Applied Physics **33**, R173 (2000).
 - [65] The wavefront distortions were measured using a high-resolution wavefront sensor, Phasics SID4-307, at Asphericon GmbH.
 - [66] J. D. Sivers and Q. Quraishi, Quantum Information Processing **16**, 314 (2017).
 - [67] Information on Sandia National Laboratories’ High-Optical-Access trap can be found at <https://www.osti.gov/servlets/purl/1239095>.
 - [68] S. Ragg, C. Decaroli, T. Lutz, and J. P. Home, Review of Scientific Instruments **90**, 103203 (2019).
 - [69] D. Rotter, *Quantum feedback and quantum correlation measurements with a single Barium ion*, Ph.D. thesis, Universität Innsbruck (2008), Available at <https://quantumoptics.at/en/publications/ph-d-theses>.
 - [70] M. Brownnutt, M. Kumph, P. Rabl, and R. Blatt, Reviews of Modern Physics **87**, 1419 (2015).
 - [71] C. D. Bruzewicz, J. Chiaverini, R. McConnell, and J. M. Sage, Applied Physics Reviews **6**, 021314 (2019).
 - [72] Al₂O₃ 96 %, fabricated by ELCERAM a.s., Czech Republic.
 - [73] Screen printable gold conductor composition DuPont 5744R.
 - [74] Knowles Syfer 0805Y1K00102KST, maximum voltage 1 kV.
 - [75] Accu-Glass male gold pins type T-2, part number 110008.
 - [76] Lead-free solid wire solder, Harris SB61/2POP, 96 % Tin, 4 % Silver, 430 F.
 - [77] ISEG EHS 82 20p.
 - [78] Rohde & Schwarz SMC100A, option B101.
 - [79] MiniCircuits ZHL-1-2W+.
 - [80] W. Macalpine and R. Schildknecht, Proceedings of the IRE **47**, 2099 (1959).
 - [81] SmarAct SLC-1720-S-UHVT.
 - [82] Kimball Physics MCF800-SphSq-G2E4C4A16.
 - [83] VAT 54132-GE02.
 - [84] Bayard-Alpert ion gauge, Agilent UHV-24.
 - [85] SAES CapaciTorr Z400.
 - [86] SAES NEXTorrr D 100-5.
 - [87] All viewports were fabricated by VACOM GmbH and anti-reflection coated by Laseroptik GmbH.
 - [88] VACOM VPCF63DUVQ-L-LAMBDA10.
 - [89] VACOM VPCF16GE-K.
 - [90] D. R. Leibbrandt, R. J. Clark, J. Labaziewicz, P. Antohi, W. Bakr, K. R. Brown, and I. L. Chuang, Physical Review A **76**, 055403 (2007).
 - [91] S. Olmschenk and P. Becker, Applied Physics B **123**, 99 (2017).
 - [92] Custom design fabricated by AlfaVakuo e.U., Austria.
 - [93] Custom design fabricated by Testbourne Ltd, UK.
 - [94] T. G. Ballance, J. F. Goodwin, B. Nichol, L. J. Stephenson, C. J. Ballance, and D. M. Lucas, Review of Scientific Instruments **89**, 053102 (2018).
 - [95] Coherent Flare NX.
 - [96] P. Obšil, A. Lešundák, T. Pham, K. Lakhmanskiy, L. Podhora, M. Oral, O. Číp, and L. Slodička, Review of Scientific Instruments **90**, 083201 (2019).
 - [97] G. A. Araneda Machuca, *Experiments with single photons emitted by single atoms*, Ph.D. thesis, Universität Innsbruck (2019), Available at <https://quantumoptics.at/en/publications/ph-d-theses>.
 - [98] M. Steiner, H. M. Meyer, C. Deutsch, J. Reichel, and M. Köhl, Physical Review Letters **110**, 043003 (2013).
 - [99] B. Brandstätter, A. McClung, K. Schüppert, B. Casabone, K. Friebe, A. Stute, P. O. Schmidt, C. Deutsch, J. Reichel, R. Blatt, and T. Northup, Review of Scientific Instruments **84**, 123104 (2013).
 - [100] P. Lodahl, Quantum Science and Technology **3**, 013001 (2017).
 - [101] P. C. Humphreys, N. Kalb, J. P. Morits, R. N. Schouten, R. F. Vermeulen, D. J. Twitchen, M. Markham, and R. Hanson, Nature **558**, 268 (2018).
 - [102] J. Bentham, *Panopticon or the inspection house (1791)* (Kessinger Publishing, WhiteFish MT, 2009).
 - [103] G. Fontana-Giusti, *Foucault for architects* (Routledge, 2013).